RESEARCH ARTICLE

Check for updates

Oscillatory patterns in redox gradient materials through wireless bipolar electrochemistry. The dynamic wave-like case of copper bipolar oxidation†

L. Fuentes-Rodríguez, [ID] [a] E. Pujades,[a] J. Fraxedas, [ID] [b] A. Crespi,[a] K. Xu, [ID] [a] L. Abad[c] and N. Casañ-Pastor [ID] *[a]

Bipolar electrochemistry allows the development of processes in a wireless manner, with reactions occurring at the induced anodes and cathodes of an immersed conducting material in the electrolyte. As a result, a gradient oxidation state may appear along the main axis field on the surface or bulk of the material depending on the type of reaction available at each induced potential. Redox intercalation gradients have been observed, metal anodization, or deposition, and also reactions at the electrolyte in the nearby environment of the poles induced. The complex oxidation of copper and interconversion between phases formed yields in this work an oscillating redox gradient, thanks to the great resistance change when the oxidized phases are formed. Parallel stripes containing mainly Cu_2O, CuO, and $Cu(OH)_2$ with large resistance are formed perpendicular to the electric field, forming a sequence of secondary dipoles in intermediate Cu stripes, that depends on the external voltage applied, and that oscillates in time at the same spatial coordinates. With longer times, copper solubilizes at the larger induced potential zones, probably as $Cu(OH)_4^{2-}$. A simple finite element electrostatic model defines the complex potential waves induced in the piece. The resulting dynamics offer an example of the complexity of order in unwired conducting materials in wet media, either in catalysis, bioelectrodes, electronics, photovoltaics, or energy storage.

Introduction

Redox gradient materials are not usual in materials chemistry but are found in nature due to the natural geochemical processes, pressure, and time evolution or atmosphere exposition.[1–5] It is thought that such natural redox gradients are at the origin of the original amino acid synthesis.[6] On the other hand, the existence of redox gradients is at the root of charge transport in many biological processes,[7] regulates homeostasis,[5] and is desirable in photosystems for efficient charge transport cascades.[3] On the other hand, the materials science field prioritizes the search of homogenous phases, required in many characterization techniques and purity control. Significant processes like electrode

reactions involving intercalation, deposition or anodization, however, create redox gradients that are hard to characterize.[8–10] Electrochemical energy storage electrodes, mixed conductors, and photochemical systems are also relevant examples, where ionic and redox gradients and their dynamics define the final performance of devices.[9]

In parallel, synthetic wireless electrochemical processes are known to be possible through dipole induction in immersed conducting materials, in what is usually called bipolar electrochemistry.[11–13] When a conducting material is placed along the externally imposed electric field lines, it polarizes in an opposite direction to the external field, and an induced anode and cathode appear at opposite borders, which induce electrochemical reactions and may create a compositional gradient along the sample. This effect occurs for any geometries and size of the immersed material and of the electric field imposed, and how the field lines are intercepted, with different spatial effects and has rather significant applications in patterning, polymer motion, synthesis of anisotropic particles or even influencing neural cell behavior.[11–23]

The horizontal geometry simplified, in particular, yields to an oxidation at the surface of the induced anode, and a

[a] Institut of Materials Science of Barcelona, CSIC, Campus UAB, 08193 Bellaterra, Barcelona, Spain. E-mail: nieves@icmab.es

[b] Catalan Institute of Nanoscience and Nanotechnology (ICN2), CSIC and BIST, Campus UAB, Bellaterra, 08193 Barcelona, Spain

[c] Institut of Microelectronics of Barcelona-Center National of Microelectronics, CSIC, Campus UAB, 08193 Bellaterra, Barcelona, Spain

† Electronic supplementary information (ESI) available: Supplementary Material available containing XPS survey and deconvolutions, X-ray diffraction data and Comsol variables. See DOI: https://doi.org/10.1039/d2qm00482h

corresponding reduction at the induced cathode in two clearly differentiated poles on the same surface. Those reactions may be of species in the electrolyte nearby or correspond to the material itself, depending on the conditions and materials chosen. Thus, intercalation of ions has been reported in induced cathodes in iridium oxide or conducting polymers,[13,24] asymmetric electrodeposition of metals, and solvent oxidation and reduction (forming O_2 and H_2 in the case of water, with corresponding pH changes). Thus, electron transfer occurs also at the induced poles of what can be described as a bipolar electrode, and impedance changes are observed in the cell. Actual electron conduction among the poles eventually cancels the charge difference, in some cases with ionic re-equilibration.[24] In some of those cases, a redox relaxation behavior after bipolar electrochemistry has been clear. Also, along with the formation of new species and/or stoichiometries, the conductivity of the material may also be changing, which in turn may modify the point of zero charge, initially present at the center of the conducting material, or modifying the dipole initially formed.

It is also relevant that, in particular, copper applications are wide and of great interest, either in biosystems, electronics, photovoltaics, catalysis, or CO_2 reduction.[25–29] Many of those cases present redox gradients during use or require the existence of such gradient. In an attempt to elucidate the dynamics that correlate the redox gradients with the eventual changes in physical properties, our study has chosen an initially simple case, the oxidation of copper metal in wireless bipolar conditions in alkaline media. As this work describes, the formation of a gradient is nothing but simple in this case, since the formation of insulating phases creates new zones and sub-dipoles with their respective induced anodes and cathodes, resulting in a wave–like oscillation of the oxidation, along the electric field. This new type of nano- and micro-structuring is relevant from the basic point of view but also in any of the processes described above and illustrates new possibilities in materials preparation and interfaces design.

Experimental

Copper metallic sheet cut in specific square dimensions (Alfa Aesar 99.95%), and previously cleaned in 1 M HNO_3, was used in all cases as immersed metal in 1 M KOH electrolytes. Electric fields were applied using Pt sheets (rectangular 15 × 35 mm^2, immersed 6 mm in the electrolyte) as anode and cathode, placed in parallel at distances of 25 mm in a Petri dish with an electrolyte height of 6 mm. See the scheme in Fig. 1a. Cell voltages of 6 V to 12 V (corresponding to 2.4–4.8 V cm^{-1}) were applied, corresponding to previously established safe potentials in water and where the effect is observed for this geometry. The copper piece (10 × 10 mm^2) was always centred among the platinum electrodes. The expected initial voltage drop across the cell including the conducting copper piece is schematically shown in Fig. 1b. Sample cleaning after bipolar treatment was performed with deionized water, soaking three times, and drying under N_2 atmosphere. Additional media, based on chloride and
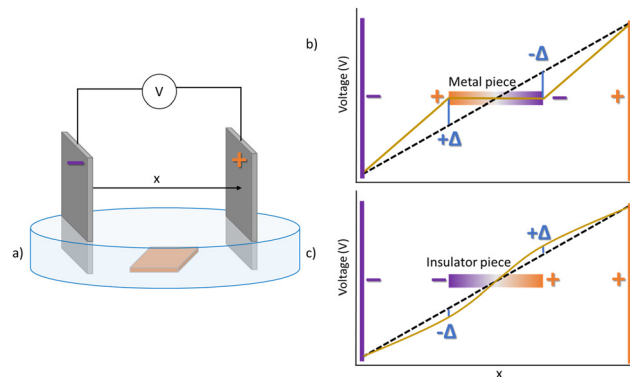

Fig. 1 (a) Cell geometry for a centred piece immersed between two parallel Pt electrodes. (b) Scheme of voltage profiles for the electrolyte (black), and for a cell with a conducting immersed copper piece under an external applied field. (c) Scheme of voltage profiles for the electrolyte (black), and for a cell with an insulating immersed piece under an external applied field. Δ values express the deviation from the electrolyte drop and contribute to the induced dipole.

phosphate electrolytes, had also been tested in prior work, and resulted in copper dissolution and/or gel formation of Cu^{+2} species, and are not shown here.

The voltage was applied either with a Biologic VSP potentiostat/galvanostat or with a VWR Perfect BlueTM 300 V power supply. Both differ in the time of reaching the set potential and create small differences among the samples, for the same voltage. Final stripes at the samples however coincide in the characterization tests.

Cyclic voltammetry of connected copper pieces in anodic and cathodic starting runs was made in 1 M KOH in order to identify the copper oxidation processes in this media, using the same potentiostat described above. The working electrode was a Cu wire, 0.5 mm in diameter, 99.9% Advent. An Ag/AgCl double bridge reference electrode (using as external solution a 3 M LiCl aqueous solution), and a Pt sheet as counterelectrode were used.

All characterization carried out on the set of stripes on samples was done *ex situ* and with spatial resolution. The nomenclature of different zones is homogenous for all characterization techniques and is based on the colour observed. Zones of the same colour are compared in different samples for reproducibility. Two batches of the same Alfa Aesar copper described above yield different greenish zone amounts. The use of a power source or a potentiostat, as described above, also induces small differences.

SEM images were obtained in a SEM QUANTA FEI 200 FEG-ESEM electron microscope. The beam position was achieved through the Motorstage EC, 50 × 50 BDM Spares controller. EDX was performed at specific zones using visual inspection of the low magnification images.

Ex situ XPS experiments were performed using a SPECS PHOIBOS150 hemispherical analyser with a monochromatic X-ray source (1486.6 eV) operated at 300 W in a base pressure of 5×10^{-10} mbar. Binding energies are referred to the 284.8 eV C1s line to correct for eventual surface charging even if the bulk

material (copper) is metallic. Since the dimensions of the X-ray spot is of about 1 mm × 3 mm, the samples have been fixed to the sample holders so that the stripes are parallel to the long dimension of the spot. The different regions are visually identified through a small aperture along the analyser cone axis pointing perpendicularly to the samples surface and selected with the help of a xyz-manipulator. However, since the short dimensions of the stripes are in the order of 0.5 mm and below, each spectrum may contain contributions from the neighbouring regions. Despite that, relative changes result obvious. Deconvolutions were performed with the CasaXPS software,[30] using Gaussian–Lorentzian line shapes and Shirley background subtraction.

X-Ray diffraction was performed using a Bruker-AXS D8 Advance diffractometer (Cu Kα$_{1,2}$) equipped with a Vantec-500 2D detector. An omega-scan with a 15[a] frame width during 900 seconds is used. With a two-dimensional detector, the diffraction is no longer limited to the diffractometer plane and a large portion of the diffraction rings can be measured simultaneously. When integrating, an area detector frame in the 2θ–χ directions a standard intensity versus 2θ diagram pattern is obtained. Since anodization occurs at the surface and causes growth of new phases, the basal plane is not homogeneous in texture and causes some shifts among peaks when the total area is integrated. Thus, Cu metal peaks have been used as reference. The incident beam is defined to go along each stripe and position was achieved using an xy table. Spectra shown are extracted from the bidimensional detector signal to facilitate representation.

RAMAN spectra were obtained at each specific zone using a Horiba–Jobin Yvon Labram HR800 spectrometer with Open-Electrode TE-cooled CCD detector, using a 514.5 nm laser and 600 l mm^{-1} grating.

Resistance measurements were carried out using a two terminal Keithley multimeter (model 2470), using round shape pins.

A simple electrostatic model was built using COMSOL Multiphysics software (version 6.0)[31] using the *Electrostatics* module, in order to explain the experimental wave-like oscillation in the oxidation of the copper sheet. We implement the simulation by applying an external voltage through the driving electrodes and accounting for the insulating boundary conditions in the geometry of experimental bipolar cell used in this work. In such module classical equations from electromagnetic theory are used, with finite boundary conditions, and no electrochemistry is defined. Thus, it corresponds to a stationary initial state. The conductivities of electrolytes and copper were obtained from literature[32,33] while the experimental measurements were used for the conductivity values of the new appearing phases (Table S1, ESI†). In the finite element model, the grid was optimized for the electrolyte interface and also for the different phases that appear on the copper surface (see the ESI† such as mesh parameters (Table S1) and a geometric illustration with the mesh used across the bipolar cell (Fig. S4)). Finally, the fitting parameters were compared to reach final convergence. Each of the calculations showed in this work corresponds to a specific snapshot related with the possible internal dipoles observed as the induced oxidation occurs as stripes.

Also, in order to emphasize the dipoles observed (each individual charge separation) a profile of V_{cell}–$V_{electrolyte}$ for each position in copper along the field axis was made, in a wide span of conductivities of the less conductive phases and for various conductive phases. Each of the calculations corresponds to a specific snapshot related with the possible dipoles observed as the induced oxidation occurs in the immersed copper. In the finite element model, the grid was optimized for the electrolyte interface and also for the different phases that appear on the copper surface, and the fitting parameters compared to reach final convergence. Finally, a comparison of the potential drop across the cell was made for various conductivities of the less conductive phase formed vs. a conductive piece (copper piece) and for various conductive phases vs. an insulating piece. The conductivities of electrolytes and copper were obtained from literature[32,33] while the experimental measurements were used for conductivities for appearing phases. A summary of other significant parameters of the calculation is shown in Table S1 in ESI.†

Results and discussion, experimental

When a conducting material is immersed in an electrolyte, upon application of an external applied field, an induced dipole is created among its borders that opposes the external field. Thus, an anode and cathode appear at opposite poles, where oxidation and reduction reactions respectively may occur, in what is known as bipolar electrochemistry. Thus, copper oxidation is expected to take place at the induced anode at the copper surface, at sufficiently high driving external potential, (Fig. 1b). Polarization then would shift towards the opposite side where the metal remains unoxidized. In contrast, if the immersed piece is insulating, only a weak perturbation of the field is observed (Fig. 1c).

As observed in Fig. 2, bipolar oxidation of copper occurs at the induced anode. However, it does not happen in a linear form, according to the induced initial potential. Significantly, in the configuration described in Fig. 1b, oxidation in form of stripes perpendicular to the field direction appear. Propagation of the oxidation front occurs from the induced anode towards the centre of the sample. This perpendicular orientation occurs always independently of the shape of the immersed copper (ex. square or circular) on the surface aligned with the field. In this work, in order to maximize the spatial dimensions of the stripes observed, an orientation along one of the diagonals of a square has been chosen (Fig. 2).

Fig. 2 shows the different evolution of wireless bipolar anodization on the copper sheet, depending on the external voltage applied between the external driving Pt electrodes, during the first 6 minutes. In all cases a brown-black zone is formed, suggesting CuO formation with small particle sizes. The formation of the dark stripe occurs after a time that is inversely proportional to the applied external potential, and reaches a larger spatial extension within the positive pole (left of the copper piece). Comparing the 8 V and 10 V cases, the
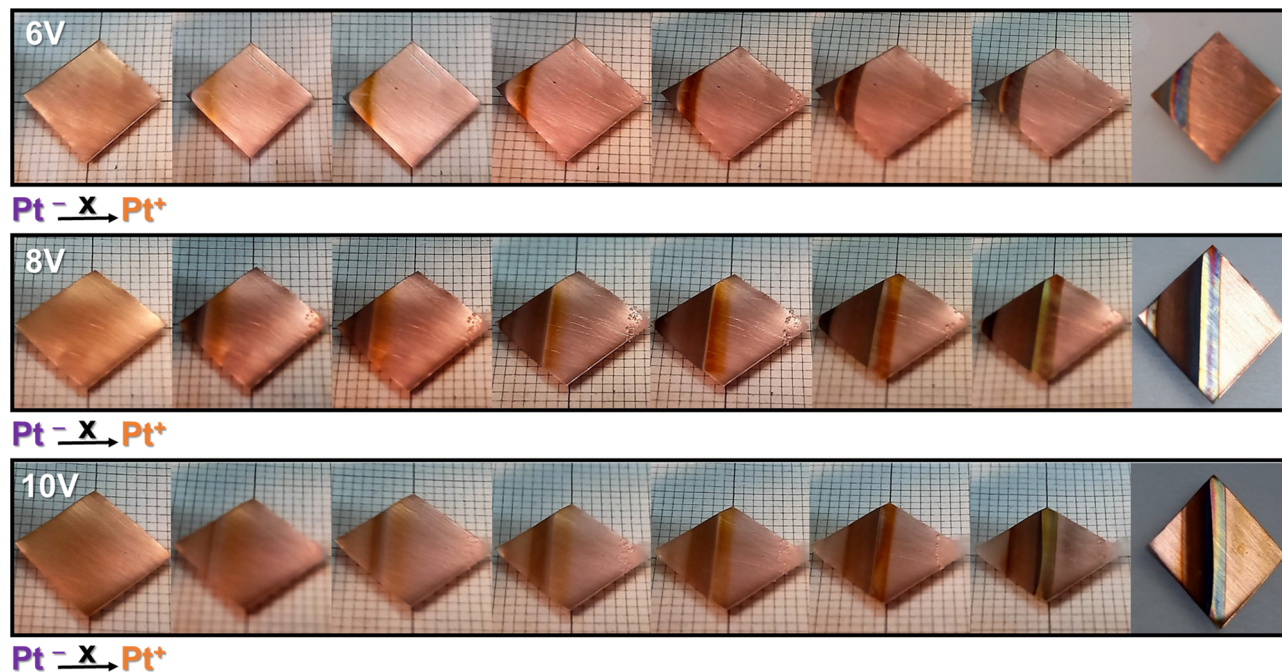
Fig. 2 Time evolution (6 min) of copper oxidation induced at 6, 8 and 10 V between Pt driving electrodes with left Pt being negative and the Pt at right being positive. The initial picture in each file corresponds to time zero and no applied potential. The last picture of each series corresponds to the piece once extracted from the solution.

final width of such black zone is larger when the applied potential is lower, but at 6 V the voltage seems to be too low for such propagation. At first sight, a longer time at 8 V bipolar treatment reaches almost the same than shorter times at larger voltage, 10 V, once such threshold is achieved. But further observations show that it is not exactly the case. Larger voltages reduce the width of the black stripes, while enhancing the dissolution of the border induced anode which has larger induced voltages. Thus, the oscillating behaviour observed visually depends greatly on the external applied voltage.

A second stripe appears simultaneously to the right, with a red colour suggesting the formation of Cu_2O, but separated by a copper colour zone, apparently unreacted. As the potential is expected to be lower moving away from the vortex, the sequence seems logical at first sight with Cu^{+2} near the positive border and Cu^+ farther away from it. But the evolution is not so obvious. Although the black zone appears initially at the vortex, where a larger potential is expected, it seems to move across the sample with time. Time evolution shows that the vortex phase dissolves, probably due to the formation of another soluble species. At larger potentials, 10 V, the vortex shows directly a clean copper colour, as if such soluble species is formed. Thus, the final sample also contains a larger clean vortex after the process, and the black zone has advanced more along the main axis of the electric field (copper diagonal). In most cases, a stripe with a bluish colour of different intensity observed by reflection is observed, mixed within the reddish-brown stripe, suggesting the formation of hydroxides or hydroxicarbonates along with oxides. It is also important to remark that the charge difference induced in these experiments has a discharge path

through the inner copper metal. However, equivalent experiments with thin layer copper deposited on TEM grids also show the same effect.

Finally, when the process stops, up to four different zones with a darker colour than the original in copper and apparently empty clean Cu stripes separating them, are found, at different positions along the axis of the sample aligned with the field. A bluish green colour also appears in some zones especially once the sample is exposed to the atmosphere, evidencing the formation of copper hydroxides or hydroxicarbonates. Experimentally, as potentials imposed are lowered (see 6 V vs. 8 V external voltage), the stripes get wider evidencing an influence of the growth rate of each insulating phase (Fig. 2).

There is some degree of variability in the position of the stripes among different copper batches used with the same commercial reference, but the results of the techniques that follow have shown reproducible results for all the zones of the same colour. The data, in each case, is accompanied by an image for easy identification, with all zones named equally across samples. Small changes in curvature of the stripes are also observed and correlated with the bending during the cut in square pieces.

SEM images (Fig. 3) evidence the original microstructure of the Cu sheet used and the growth of bundled fibres in the Z4 zone, corresponding to the black stripe. Also, the Z3 zone shows the appearance of microcrystals with smaller size than those of Z4. Inner stripes are also found within Z4 zone (Fig. 3b)

A first evaluation of the chemical changes due to bipolar treatment comes from the ex situ study of the relative oxygen content, through EDX, along the main axis of the sample
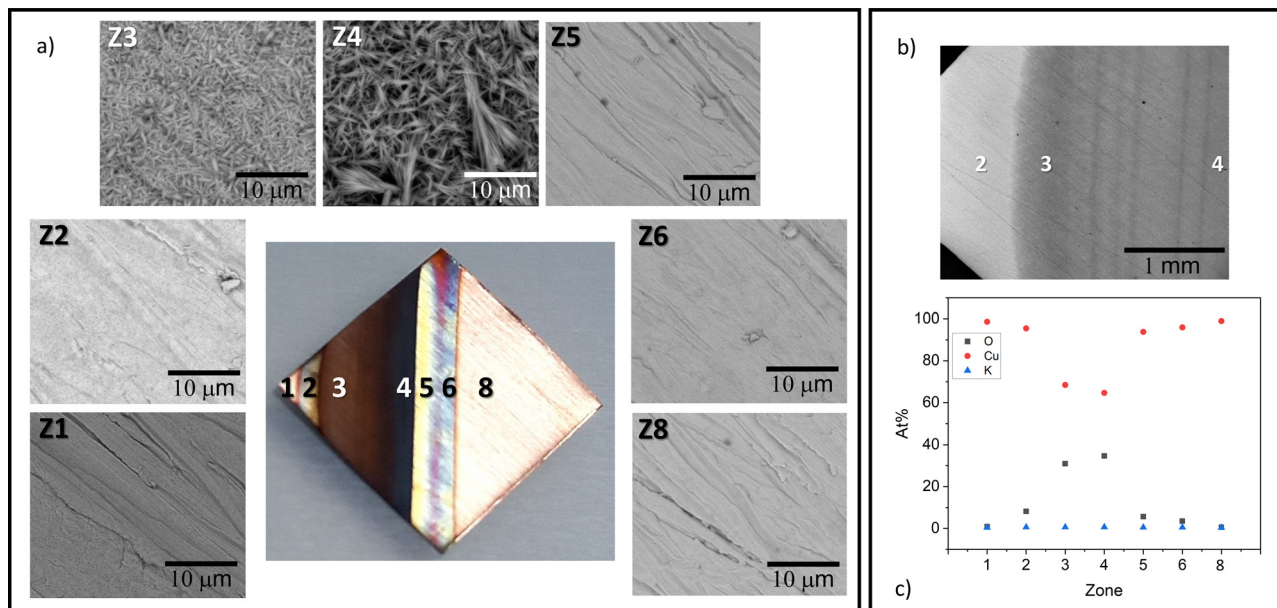
Fig. 3 (a) SEM images with spatial resolution corresponding to the different zones marked in the optical image for a copper sample treated using 8 V external voltage. (Please note that roughness exists in the original as purchased Cu foil.) (b) Detail SEM images with lower resolution showing internal stripes at zone Z4. (c) EDX relative change in O, K and Cu content. (Please note that the signal from underlying metallic Cu shifts the global copper %, and therefore the y axis is arbitrary. Also note that the K constant small value suggests a small degree of contamination from the solvent.)

(Fig. 3c). In it, it is obvious that regions Z3 and Z4 have the largest O/Cu ratios, although a small increase in oxygen is also observed for Z2, Z5 and Z6. Surprisingly oxygen content at Z2 is smaller than at Z3 and Z4. No stoichiometry is extracted from such values since the underlying copper sheet is contributing to the signal and O sensitivity is low.

Thus, the original visualization of this process including the obvious variation of oxygen stoichiometry seen in EDX, suggests that the degree of copper oxidation follows an unusual pattern in space, and contains several redox processes. In order to evaluate the number of processes, a CV on a directly connected Cu piece was run. Two different modes were explored, directly on the pristine sample towards anodic processes, or initiating the CV with a reduction that could eliminate the Cu_2O present always at the Cu surfaces (see Fig. 4).

Fig. 4a shows that if the scan starts with reduction, two small almost non observable waves, appear at E −0.7 V and −1.15 V *vs.* Ag/AgCl, which may correspond to the reduction of surface Cu_2O to metallic Cu. The small intensity in such waves is thought to be related to the small amount of Cu_2O endemically present at the surface of Cu, (see inset in Fig. 4a). The corresponding return oxidation shows a small wave at −0.4 V and two larger waves at −0.2 V and −0.1 V *vs.* Ag/AgCl. An additional wave is observed at 0.9 V *vs.* Ag/AgCl overlapped with water oxidation.

If the scan starts directly towards oxidation, similar waves are obtained, but the first oxidation near −0.4 V *vs.* Ag/AgCl is shifted and has lower intensity, while the larger waves at −0.2, and −0.1 and 0.9 V *vs.* Ag/AgCl having larger intensity, as also occurring for water oxidation. The cathodic return has two small waves at 10.5 and −0.7 V *vs.* Ag/AgCl, and show that no
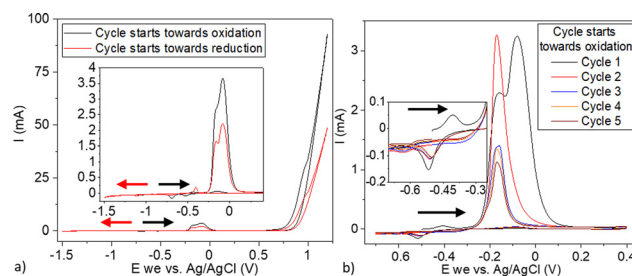

Fig. 4 (a) Copper CV started in both oxidation direction (black) and reduction direction in the available water range from the open circuit potential (−0.5 V *vs.* Ag/AgCl) using scan speed of 20 mV s^{-1}; (b) sequential CV in the smaller range not reaching water splitting waves. Scans start at open circuit potential and are run towards oxidation, using scan speed of 20 mV s^{-1}.

reversibility exists for the large waves at −0.2 and −0.1 V *vs.* Ag/AgCl. While the smaller waves in the initial scans are probably related to the reduction of Cu_2O or its formation from Cu, we observed several processes at larger overpotentials that may involve in principle larger oxidation states and not a single one corresponding to CuO.
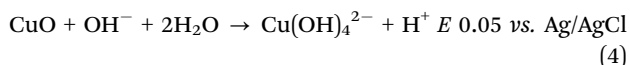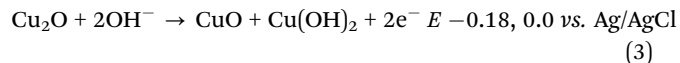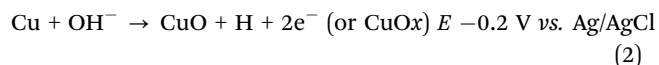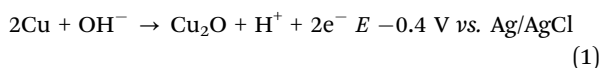
Also, the existence of a wave overlapped with water oxidation suggests a larger oxidation state for copper, possible irreversibility, and a change in pH derived from O_2 formation. Thus, Fig. 4b shows a scan within a more limited voltage range, and with several scans that may determine which processes are not reversible. The anodic peak at −0.4 V *vs.* Ag/AgCl assumed to be the formation of Cu_2O, appears only in the first scan. Then, the two large waves at −0.2 and −0.1 V *vs.* Ag/AgCl are shown to be irreversible, and only the small reduction wave, previously seen
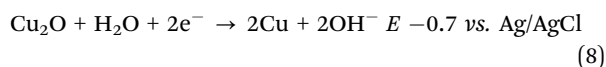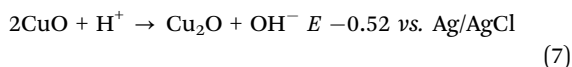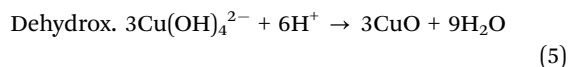
at -0.5 V, is seen. Intrinsically, it is clear that the oxidation of copper beyond Cu_2O is irreversible, even if the potential of 0.9 V near H_2O oxidation is not reached, probably because the phases formed include Cu_2O, CuO, $Cu(OH)_2$ and are much more insulating or because some phases detach or solubilize. Of interest is to observe how the two large waves coalesce in the second scan while several waves coexist at similar potentials in consecutive scans. Despite those observations, the main CV waves do not shift, and therefore, no change in pH is detected. Once more, the oxidation of copper seems to be complex, even on the same connected surface.

Previous reports from literature[34–45] for direct contact electrochemical oxidation of copper electrodes in alkaline aqueous solutions are similar, although some contradictions also exist. In general, up to four oxidation waves and two reduction waves are observed, with complex mechanisms and interconversion among several species, including formation of $Cu(OH)_2$ at lower potentials than Cu_2O, and the $Cu(OH)_4^{2-}$ adsorbed soluble species being proposed along with simultaneous reduction of CuO and Cu_2O to Cu, and dehydroxilation of the tetrahydroxide to oxides. A simple scheme, in increasing potential, may be summarized as follows:

Anodic waves (positive current)

$$2Cu + OH^- \rightarrow Cu_2O + H^+ + 2e^- \quad E\ -0.4\ V\ vs.\ Ag/AgCl \tag{1}$$

$$Cu + OH^- \rightarrow CuO + H + 2e^-\ (or\ CuOx)\ E\ -0.2\ V\ vs.\ Ag/AgCl \tag{2}$$

$$Cu_2O + 2OH^- \rightarrow CuO + Cu(OH)_2 + 2e^-\ E\ -0.18,\ 0.0\ vs.\ Ag/AgCl \tag{3}$$

$$CuO + OH^- + 2H_2O \rightarrow Cu(OH)_4^{2-} + H^+\ E\ 0.05\ vs.\ Ag/AgCl \tag{4}$$

Cathodic waves (negative current)

$$Dehydrox.\ 3Cu(OH)_4^{2-} + 6H^+ \rightarrow 3CuO + 9H_2O \tag{5}$$

$$2Cu(OH)_4^{2-} + 2e^- \rightarrow Cu_2O + 4H_2O \tag{6}$$

$$2CuO + H^+ \rightarrow Cu_2O + OH^-\ E\ -0.52\ vs.\ Ag/AgCl \tag{7}$$

$$Cu_2O + H_2O + 2e^- \rightarrow 2Cu + 2OH^-\ E\ -0.7\ vs.\ Ag/AgCl \tag{8}$$

Also, in our opinion, non-stoichiometric oxides cannot be discarded and other mixed valence phases such as CuO_x, K_xCuO_2 and Cu_4O_3, with mixed oxidation states, or copper hydroxicarbonates due to possible absorption of CO_2, may be formed and are not discarded in this study.

It is worth remarking here that cyclic voltammetry on a connected copper piece does not represent the actual bipolar potential distribution. All processes in a CV involve a change on the surface influencing the next process, while in a bipolar configuration, high potentials are available without the previous scan at lower potentials, modifying the possible mechanism

acting. Still, the information from the voltammetry is a good hint of the possible processes. We consider in this work that the same type of processes should be possible, but, as an induced bipolar system is set, the copper surface is subject to a potential gradient, and therefore the induced anode surface is initially subject to each of the oxidizing potentials. Despite this simultaneous presence of several potentials in the bipolar electrode, we may consider that the potentials observed in CV are reached for each of the processes present.

The characterization by XPS and X-ray diffraction of the stripes formed on Cu may offer additional information on the oxidation states achieved at each position in the main field axis. In the initial conditions, the larger potential at the induced anode will be at the vortex closer to the negative Pt driving electrode, (see Fig. 1 and 2), and should be decreasing if moving away from that position towards the centre of the Cu piece. Therefore, the phase formed at the corner should require a larger potential, while the phases formed at longer distances from the pole require a smaller potential, and would have lower oxidation states expected.

Fig. S1 (ESI†) shows the survey XPS spectra of the analysed regions, namely Z1, Z2, Z4, Z5, Z6, and Z8, as well as that of a reference clean, (Ar sputtered), metallic Cu(111) single crystal surface measured in the same XPS system. The main XPS and Auger lines are identified. Apart from the lines associated to copper, we observe the presence of carbon, oxygen and potassium in all regions as well as negligibly small traces of silicon and nitrogen. The presence of K in the general spectra suggested occluded traces of the solvent. However, additional soaking in water induced additional carbonation. The comparison with the clean Cu(111) references helps to visualize the signatures from carbon and oxygen species. From the figure we can conclude that the surfaces are clean after the electro–oxidation process in water and unavoidable exposure to the atmosphere, apart from endemic carbonate (resulting from CO_2 adsorption) or remnant potassium.

Fig. 5a–d show high-resolution XPS spectra of the C1s, O1s, Cu2p and CuLMM lines, respectively, for the same regions discussed in the XPS survey (Fig. S1, ESI†). At first sight, the zone Z4 is clearly distinguishable from the rest in the Cu 2p XPS spectra. The Cu2p line of Z4 is clearly differentiated from the rest with an extra line centred around 935 eV and a satellite at higher energy that may correspond mainly to Cu(ii) hydroxides and to a lesser extent to carbonates,[46–48] since it correlates with an O 1s signal typical of OH^- and CO_3^{2-} groups. The rest of regions exhibit a dominance of Cu_2O at the surface (with various thicknesses of Cu_2O possible) with a binding energy of the main peak, located at 932.2 eV[48] an energy sufficiently separated from the 932.6 eV (metallic copper) and from 933.8 eV (CuO). Fig. 5d further confirms the dominance of Cu_2O at the surface (main feature at 916.9 eV kinetic energy) with some contribution from the subsurface metallic copper foil (see feature at 918.6 eV). Contributions from hydroxides and carbonates are expected around 916 eV, thus at lower energy than that corresponding to Cu_2O, and indeed, for region Z4 a shoulder appears in that energy range. The main feature
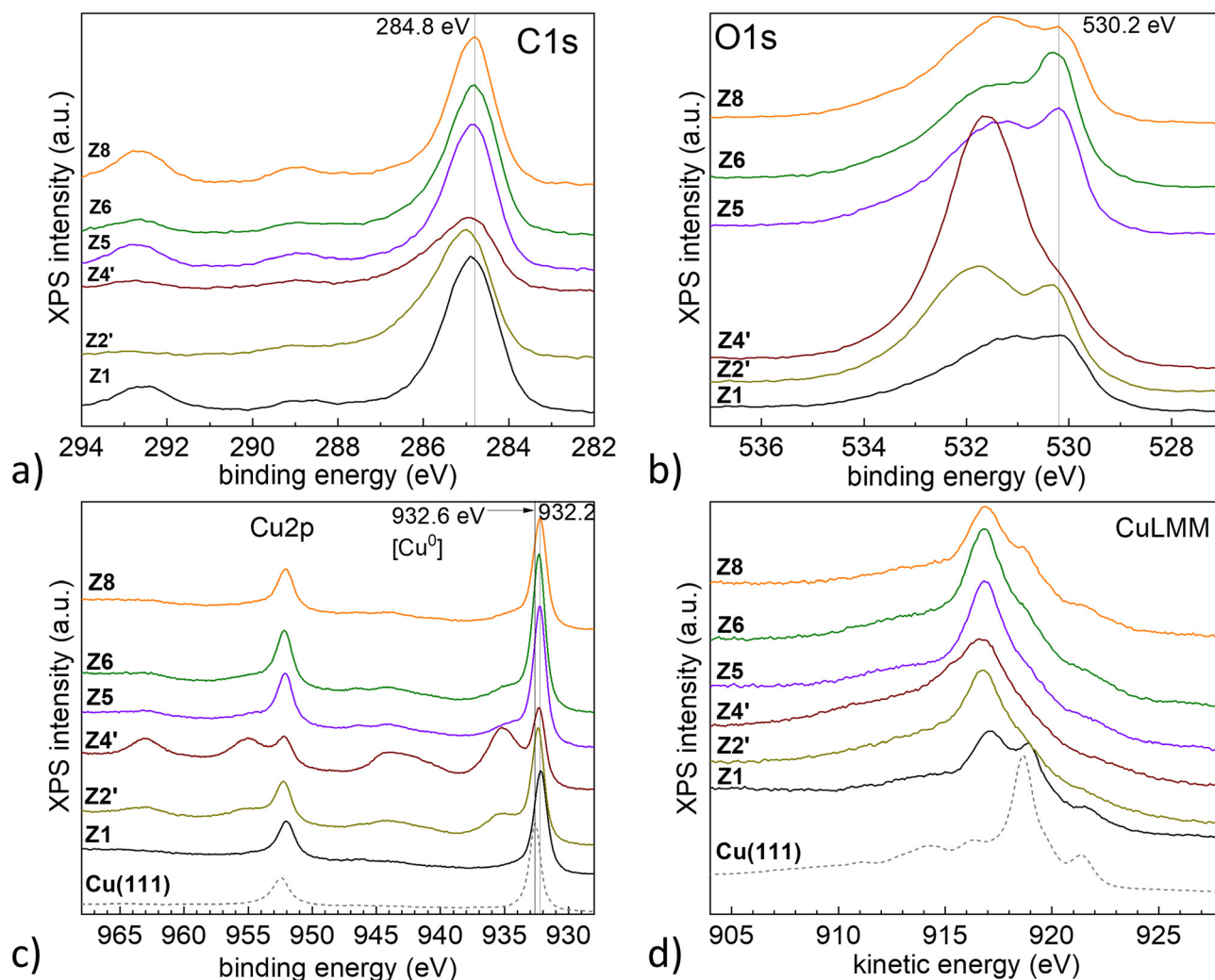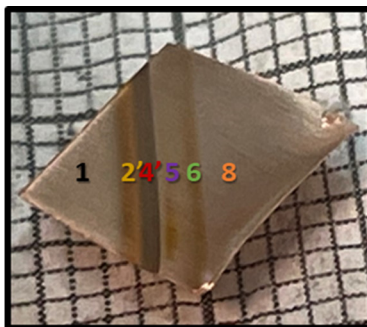
Fig. 5 High resolution (a) C1s, (b) O1s, (c) Cu 2p and (d) CuLMM spectra for the various zones described in image. Sample shown has been treated using 8 V external field. Other voltages reproduce results. Please note that zones 2 and 4 may contain zones 4 and 2 respectively since the incident beam (0.8–1 mm) is wider than the stripes (near o smaller than 5 mm). Z2′ and Z4′ correspond to an additional sample.

associated to CuO should be centred at 918 eV but no clear feature is observed at this energy. From the Auger lines, we cannot exclude the CuO phase in Z4, but if present, O1s shows that it would be in small amount and accompany a copper hydroxide species, in agreement with the Cu2p spectra from Fig. 5c.

The colour of each stripe is indeed a valuable complementary evidence, since stochiometric phases are known to have specific absorptions, and thus black represents an evidence of non-stoichiometry or of CuO, but may also hinder visualization of less coloured phases. Thickness, microstructure and particle size are also significant in that sense. Thus, despite the colour differences, Z5, Z6 and Z8 are similar at first sight in XPS, evidencing the existence of Cu_2O probably in different amounts, but Z6 also shows, when dried in atmosphere, a different degree of bluish green colour and brilliant effect that may agree with

the simultaneous formation of copper hydroxides, hydroxicarbonates or extraction of chromium as oxide to the surface. The potential presence of some impurities has been checked but has not been observed. Thus, for example, Cr would be masked by the intense Cu L3M45M45 Auger line at about 570 eV in Fig. S1 (ESI†). XPS is a helpful tool in that sense, evidencing hydroxide species as described below, and also the endemic presence of carbonates in the sample. It also evidences the existence of Cu_2O species on spatial coordinates to the left and right of the main Cu^{+2} species, $Cu(OH)_2$ and possibly (see X-ray data), CuO.

At the same time, the border where the initial induced anode exists, a high potential zone, is black in initial stages but ends up showing only the Cu metal signals for 8 and 10 V external applied voltages, possibly involving an oxidation that yields to the copper tetrahydroxide anion species, as described in literature.[41]

Deconvolution, considering other reports,[40–52] as summarized in Fig. S2, (ESI†) confirms that the most relevant changes correspond to region Z4, with $Cu(OH)_2$ formation, while Cu_2O or Cu (intermediate clean stripes) predominate in other zones, with different thicknesses. CuO cannot be discarded from the XPS data given the surface sensitivity of the technique. Carbonates and hydroxicarbonates are probably present in some extent due to CO_2 exposure.

X-Ray diffraction patterns obtained with a linear GADD detector result in complementary results. Fig. S3 (ESI†) (global diffraction pattern) and Fig. 6 (magnified peaks) show the crystalline phases that can be observed in each of the regions, with standard incidence angles, and aligning the incident beam along the stripe. Since anodization occurs at the surface and causes growth of new phases, the basal plane is not homogeneous and causes some shifts among peaks.

Along with the omnipresent Cu diffraction lines several indexed phases appear at each zone. Cu, Cu_2O, CuO and $Cu(OH)_2$ are indicated by the several coloured lines.[53] When a greenish phase appears, no differences are observed. While endemic Cu_2O is present even in pristine Cu zones, the Z4 zone is the one where more changes are observed, as XPS data also had shown. CuO and $Cu(OH)_2$, easily interconverted, are present in Z4, while it is the only zone where the $Cu(OH)_2$ phase is seen. Indexing of additional crystalline phases as Cu_4O_3 and hydroxicarbonates has been attempted with no success, but their existence or other amorphous phases cannot be discarded.[53] Oxidation of impurities present in Copper (50 ppm maximum on Cr for example) that could get extracted at the surface, have also been investigated but no evidence of them exists in X-ray diffraction.

Local resolution Raman spectra (Fig. 6b) confirms the existence of Cu (300 cm^{-1}), Cu_2O, (peaks at 644, 216 and 148 cm^{-1}) and $Cu(OH)_2$ (peaks at 288, 450, 489 cm^{-1}) and CuO (peaks at 288 cm^{-1}) although some of the peaks are common to the last two phases.[54,55] (It is remarkable the large crystallinity of the peak at 490 cm^{-1} corresponding to $Cu(OH)_2$. It is also evident the sequence of oxidation states for Cu across the different zones.

Thus, chemical identification is in agreement with the formation of insulating or large band gap semiconductor oxides and
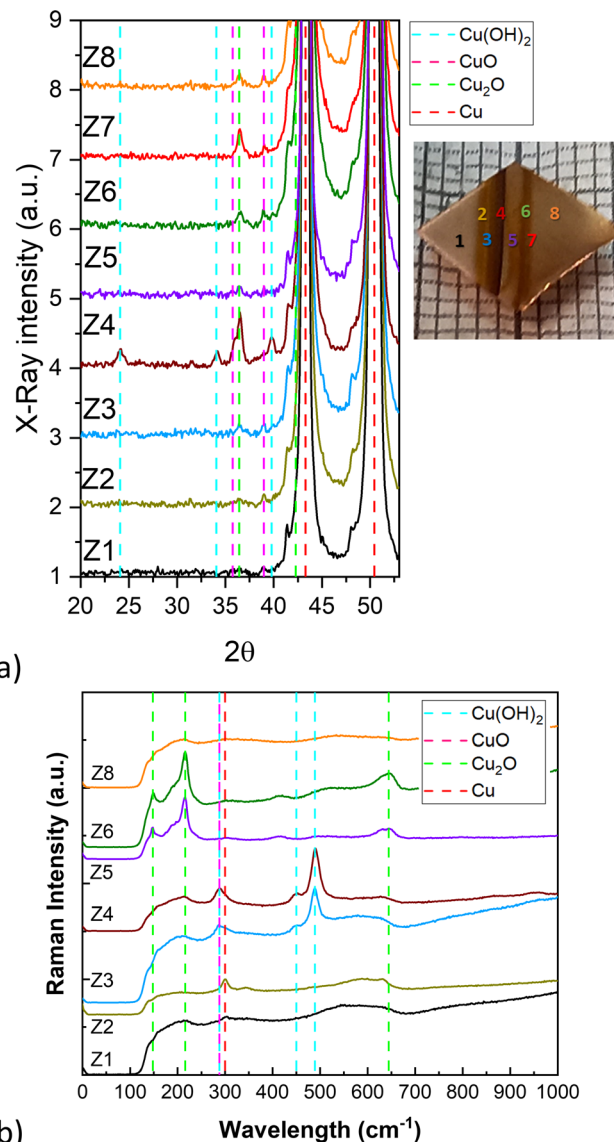

Fig. 6 (a) X-ray diffraction patterns extracted from GADDs diffractometer in each of the lines, and indexation. Spectra correspond to a sample treated at 8 V external voltage. Other voltages reproduce results. The global diffraction pattern is shown in Fig. S3 (ESI†). (CuO: PDF 00-001-1117; Cu_2O: PDF 01-077-0199; Cu: PDF 00-004-0836; $Cu(OH)_2$: PDF 00-35-0505, ICDD PDF4+ 2022 database[53]). (b) Raman spectra for different zones.

hydroxides at the copper surface in alternating oxidation states, in a complex behaviour that occurs sequentially in direct contact electrodes, but simultaneously in bipolar electrochemistry configurations. As expected from the chemical identity of the phases, a simple two contact measurement, shows that all are more insulating than the starting copper metal, with Cu, and oxidized brown and black zones yielding values in the ranges of 10^1 Ω, 10^4 Ω and 10^6 Ω respectively. These values are in agreement with the data span usually reported for copper oxides[56,57] and with the presence of copper hydroxide plus the microstructure of CuO electrochemically grown.

From a purely electrostatic approach, the appearance of new phases with larger resistivity modifies the piece conductivity

and also the local field distribution, generating changes in the induced dipoles. In a simple case of a metal forming a single insulating oxide, the anode part becomes insulating, and only the remaining conducting surface gets polarized, thus shifting the point of zero charge towards the cathode. That occurs despite the underlying conducting material.[24] However, the existence of several insulating phases formed in copper may yield to a different case, as in this case. Thus, given the change in conductivity of the surface observed, an evaluation of the critical parameters that may modify the original dipole induced is of interest. That has been done simulating, through a COMSOL finite element approach, the voltage profile on copper for various unknown phases of different conductivity being formed during oxidation.

As described in Fig. 7a, for the same conductivity of the electrolyte (1 M KOH, 17.8 S m^{-1},[32,33]) different conductivities of the new phases formed generates induced anodes with different potentials, with significant changes appearing at the induced anode. A critical change is observed when the difference between the electrolyte conductivity and the material conductivity reaches a difference of two orders of magnitude. Thus, a threshold exists where the resulting potential changes sign from the original positive found for copper conductivities to a negative value, expected for insulating materials (see Fig. 1b and c).

Since the actual potential of the induced cathode and anode is related with the deviation of the potential with respect to the electrolyte voltage drop as shown in Fig. 1b, the plots on Fig. 7 are given as the difference between the calculated voltage and the electrolyte voltage at that point. For easy comparison, also modifications of the conductivity at the induced cathode are shown in Fig. 7b, although all evidence suggests only metallic copper is present at that spatial coordinate. As the conductivity of the material at the induced cathode is decreased, also decreases the intensity of the induced potential. Thus, the combination of both calculations suggest already that a central

stripe could appear with a positive and larger potential that the potential at each border of the copper piece. Furthermore, an inversion in the sign of the anode pole voltage may occur. Experimental data compared with that simulated screening of conductivities suggests that for insulating phases with conductance between 10^{-5} and 10^{-10} S m^{-1}, a dipole change is expected to be substantial, since electrolyte conductivity is 17.8 S m^{-1} at 20 °C,[32,33] a resistance smaller in two orders of magnitude than the insulating phases (see Fig. 7a, for the smaller conductivity case).

On the basis of this calculation and the patterns observed experimentally, a simulation based on each snapshot of the formation of stripes observed during oxidation has been done using COMSOL single element electrostatic model. Each stripe taken into account in the model has the resistance that was measured experimentally. Fig. 8 shows the scheme of stripes (line 1), and the simulated isopotential curves (line 2), charge distribution (line 3) and voltage profiles (line 4) for the evolution patterns observed visually.

As observed in Fig. 8, COMSOL simulations may explain the existence of secondary dipoles within the Cu oxidized surface. As an insulating zone appears by oxidation, a possible barrier is suspected and a new dipole appears behind. After a first insulating phase appears on the copper surface, a new created dipole appears behind and the b situation appears. The induced secondary dipoles in the new zone are not, however, of the same intensity, since the distance to the driving Pt electrode has increased and the screening of previous insulating zones has appeared, but it retains the same direction than the original one, opposing the external field. Thus, a positive induced potential (secondary anode) is lowered in the second conducting zone. It is relevant that also the negative reduction pole on the opposite border of the new sub-dipole is quantitatively smaller (see part 4b in Fig. 8). As other new stripes appear, up to three voltage maxima appear, all of smaller intensity than the original calculated for metallic copper, explaining the appearance of consecutive parallel stripes.
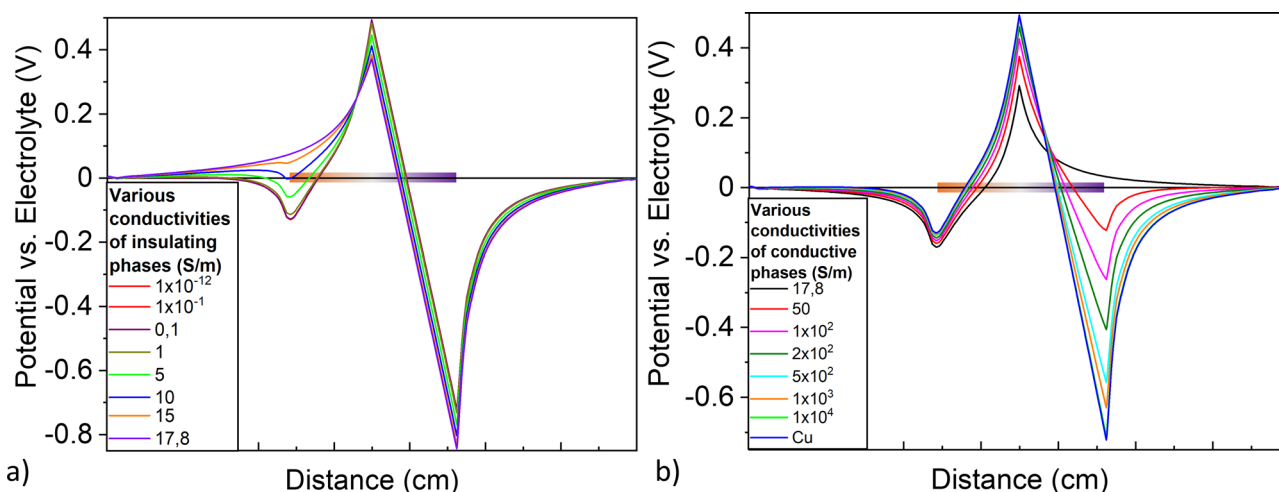

Fig. 7 (a) Simulation of Potential profiles (Induced voltage–electrolyte voltage) across the cell (sample shaded at the center) for various conductivities of the oxidized phases formed as compared with the original dipole formed (black maximum potential difference). For easy comparison (b) shows the voltage profile for the existence of conducting parts at the induced cathode, with several conductivities.
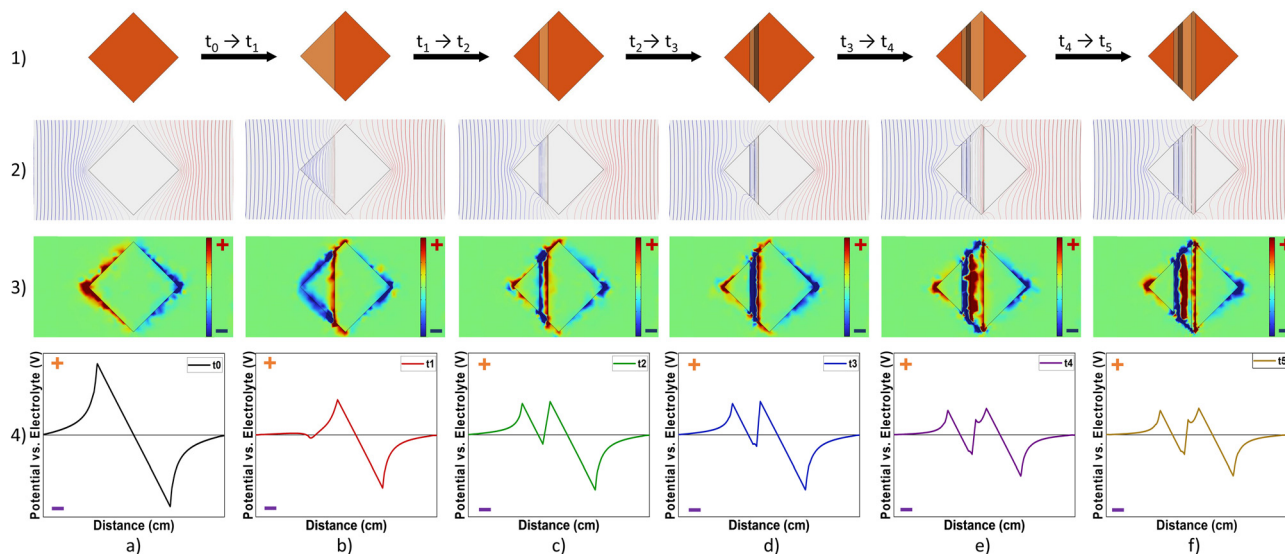
Fig. 8 COMSOL finite element modelling of each of the zones detected, assuming insulating phases being formed in different stages. Rows correspond to the (1) visual scheme, (2) isopotential lines, (3) charge distribution and (4) linear voltage profile along the main axis of the electric field for each time.

Thus, COMSOL finite element simulations allows us to give a simple model to understand the dynamic evolution of waves or oscillations as new oxidation zones appear on the copper surface with high resistance. As observed in Fig. 7 and 8, the alternance of positive and negative zones induced after insulators appear, shifts the maximum induced potential towards the center of the sample, yielding smaller positive potential, but also induces negative zones where originally a positive potential was appearing, which may induce the reduction of previously oxidized copper. Thus, we observe metallic copper stripes between oxidized copper stripes, as observed visually and in XPS and X-ray diffraction. In our experiments up to four zones are detected but also the starting of a new patterns of secondary dipoles in each zone, as stripes of insulating phases appear in a singular agreement with finite element electrostatic modelling (see Fig. 9).

Such simulations, based on the experimental observations, may also be visualized as the interference between the voltage drop across the insulating stripes and the dipoles induced at the conducting stripes since the insulating phases align with the external field and conducting parts oppose to the external field. The alternance of polarization and charge distribution yields to a dynamic sequence, of what may be simplified as resulting dipoles, all with lower magnitude than the one found at initial t0, and to a time evolution switching between positive and negative induced charges (Fig. 9). Such space and time oscillation induces oxidation and consecutive reduction at the same spatial coordinates, yielding a space and time oscillating behaviour.

As a summary, the formation of insulating phases at different potentials, yields, even at the starting point, different border lines that create new secondary dipoles of different intensity within the surface dimensions, shifting the front of the bipolar effect. At some space coordinates, the sign is opposite
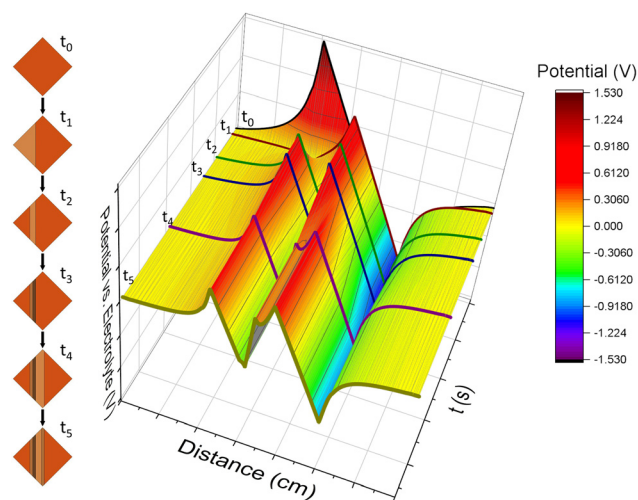

Fig. 9 Time and space evolution of the simulated potential profile at the copper surface, as oxidized insulating phases are formed. Each time step, t_0 to t_5, relate to the images placed on the left side. Please note that sample spatial dimensions are delimited by t_0 potential maxima.

to the initial setting yielding to an interference pattern in potential and a final oscillation in the copper oxidation state. At longer times, the pattern seems to reproduce again along the spatial axis within the field, and stops due to the existence of an induced cathode and the finite dimensions of the copper piece.

The appearance of such significant oscillations with a simple imposed external field is relevant to many cases where gradients are involved as part of the process. From electrodes in electrochemical energy storage systems to biological redox processes or catalysis, a possibility arises on the possible mechanisms acting, and the patterns that may induced specific redox reactions. The same simple nature that modulates such behaviour is an awakening scientific reminder of the need to

account for oscillation in synthesis, characterization, device design and applications in general.

Conclusions

Induced dipoles on conducting materials like copper allow the formation of redox gradient patterns in wireless bipolar electrochemistry, that do not appear with direct contact electrochemistry. That is so because of the change in resistivity at the surface when oxidized phases appear. The oscillating pattern, resulting in the redox gradient, derives from the appearance of secondary dipoles in the new conducting zones, and the interference between voltage jumps at insulating and conducting zones. An inner structure also exists that will be explored further. Such an order in the redox gradient has implications in electronics, corrosion, bioelectrodes, or systems where the gradient is basic for the device like photovoltaics.

Author contributions

The present work is based on an original idea on bipolar electrochemistry redox gradients by NCP, and on a very fruitful discussion on possible secondary dipoles (NCP and LA). The experimental work was originally started by EP. LFR has performed the electrochemical work as part of her thesis. COMSOL calculations have been discussed by those three main authors, and performed by LFR. AC and JF have suggested the best way of elucidating diffraction and XPS respectively with spatial resolution and have analysed the data and KX has performed spatial resolution Raman spectra.

Conflicts of interest

There are no conflicts to declare.

Acknowledgements

Notes and references

1 W. Martin, J. Baross, D. Kelley and M. J. Russell, Hydrothermal vents and the origin of life, *Nat. Rev. Microbiol.*, 2008, **6**, 805–814.

2 M. J. Russell and A. J. Hall, *The onset and early evolution of life. Evolution of Early Earth's Atmosphere, Hydrosphere, and Biosphere—Constraints from Ore Deposits*, ed., S. E. Kesler, H. Ohmoto, Geological Soc. of America, Boulder, CO, 2006, vol. 198, pp. 1–32.

3 M. J. Russell, L. M. Barge and R. Barthia, *et al.*, The drive to life on wet and icy worlds, *Astrobiology*, 2014, **14**, 308–343.

4 V. Sojo, B. Herschy, A. Whicher, E. Camprubí and N. Lane, The origin of life in alkaline hydrothermal vents, *Astrobiology*, 2016, **16**, 181–197.

5 O. Husson, Redox potential (Eh) and pH as drivers of soil/plant/microorganism systems: a transdisciplinary overview pointing to integrative opportunities for agronomy, *Plant Soil*, 2013, **362**, 389–417.

6 L. M. Bargea, E. Floresa, M. M. Baumb, D. G. VanderVeldec and M. J. Russella, Redox and pH gradients drive amino acid synthesis in iron oxyhydroxide mineral systems, *Proc. Natl. Acad. Sci. U. S. A.*, 2019, **116**, 4828–4833.

7 M. Wikström and R. Springett, Thermodynamic efficiency, reversibility, and degree of coupling in energy conservation by the mitochondrial respiratory chain, *Commun. Biol.*, 2020, **3**, 451.

8 R. Bhosale, J. Mısek, N. Sakai and S. Matile, Supramolecular n/p-heterojunction photosystems with oriented multicolored antiparallel redox gradients (OMARG-SHJs), *Chem. Soc. Rev.*, 2010, **39**, 138–149.

9 R.-C. Masse, C. Liu, Y. Li, L. Mai and G. Cao, Energy storage through intercalation reactions: electrodes for rechargeable batteries, *Natl. Sci. Rev.*, 2017, **4**, 26–53.

10 D. PLetcher and F. C. Walsh, *Industrial Electrochemistry*, Springer Sc, 1993.

11 S. O. Krabbenborg and J. Huskens, Electrochemically generated gradients, *Angew. Chem., Int. Ed.*, 2014, **53**, 9152–9167.

12 G. Loget, D. Zigah, L. Bouffier, N. Sojic and A. Kuhn, Bipolar Electrochemistry: From Materials Science to Motion and Beyond, *Acc. Chem. Res.*, 2013, **46**, 2513–2523.

13 N. Shida, Y. Zhou and S. Inagi, Bipolar Electrochemistry: A Powerful Tool for Electrifying Functional Material Synthesis, *Acc. Chem. Res.*, 2019, **52**, 2598–2608.

14 L. Koefoed, S. U. Pedersen and K. Daasbjerg, Bipolar electrochemistry—A wireless approach for electrode reactions, *Curr. Opin. Electrochem.*, 2017, **2**, 13–17.

15 G. Tisserant, Z. Fattah, C. Ayela, J. Roche, B. Plano, D. Zigah, B. Goudeau, A. Kuhn and L. Bouffier, Generation of metal composition gradients by means of bipolar electrodeposition, *Electrochim. Acta*, 2015, **179**, 276–281.

16 S. Inagi, Fabrication of gradient polymer surfaces using bipolar electrochemistry, *Polym. J.*, 2016, **48**, 39–44.

17 T. M. Braun and D. T. Schwartz, Localized Electrodeposition and Patterning Using Bipolar Electrochemistry, *J. Electrochem. Soc.*, 2015, **162**, D180–D185.

18 Z. Fattah, P. Garrigue, V. Lapeyre, A. Kuhn and L. Bouffier, Controlled Orientation of Asymmetric Copper Deposits on Carbon Microobjects by Bipolar Electrochemistry, *J. Phys. Chem. C*, 2012, **116**, 22021–22027.

19 Y. Ishiguro, S. Inagi and T. Fuchigami, Gradient Doping of Conducting Polymer Films by Means of Bipolar Electrochemistry, *Langmuir*, 2011, **27**, 7158–7162.

20 S. E. Fosdick, K. N. Knust, K. Scida and R. M. Crooks, Bipolar Electrochemistry, *Angew. Chem., Int. Ed.*, 2013, **52**, 10438–10456.

21 Y. Zhou and D. L. Engelberg, Fast testing of ambient temperature pitting corrosion in type 2205 duplex stainless steel by bipolar electrochemistry experiments, *Electrochem. Comm.*, 2020, **117**, 106779.

22 N. Karimian, P. Hashemi, A. Afkhami and H. Bagheri, The principles of bipolar electrochemistry and its electroanalysis applications, *Curr. Opin. Electrochem.*, 2019, **17**, 30–37.

23 A. M. Rajnicek, Z. Zhao, J. Moral-Vico, A. M. Cruz, C. D. McCaig and N. Casañ-Pastor, Controlling Nerve Growth with an Electric Field Induced Indirectly in Transparent Conductive Substrate Materials, *Adv. Healthcare Mater.*, 2018, **7**, 1800473.

24 L. Fuentes-Rodríguez, L. Abad, L. Simonelli, D. Tonti and N. Casañ-Pastor, Iridium Oxide Redox Gradient Material: Operando X-ray Absorption of Ir Gradient Oxidation States during IrOx Bipolar Electrochemistry, *J. Phys. Chem. C*, 2021, **125**, 16629–16642.

25 R. A. Festa and D. J. Thiele, Copper: an Essential Metal in Biology, *Curr. Biol.*, 2011, **21**, R877–R883.

26 Z. Chen and T. J. Meye, Copper(II) Catalysis of Water Oxidation, *Angew. Chem.*, 2013, **125**, 728–731.

27 S. Popovic, M. Smiljanic, P. Jovanovič, J. Vavra, R. Buonsanti and N. Hodnik, Stability and Degradation Mechanisms of Copper-Based Catalysts for Electrochemical CO_2 Reduction, *Angew. Chem., Int. Ed.*, 2020, **59**, 14736–14746.

28 K. Vijayan, S. P. Vijayachamundeeswari, K. Sivaperuman, N. Ahsan, T. Logu and Y. Okada, A review on advancements, challenges, and prospective of copper and non-copper based thin-film solar cells using facile spray pyrolysis technique, *Sol. Energy*, 2022, **234**, 81–102.

29 T. P. Nicholls and A. C. Bissember, Developments in visible-light-mediated copper photocatalysis, *Tetrahedron Lett.*, 2019, **60**, 150883.

30 J. Walton, P. Wincott, N. Fairley and A. Carrick, *Peak Fitting with CasaXPS*, Accolyte Science, Knutsford, UK, 2010.

31 COMSOL Multiphysics® v. 6.0. www.comsol.com. COMSOL AB, Stockholm, Sweden.

32 R. J. Gilliama, J. W. Graydonb, D. W. Kirkb and S. J. Thorpe, A review of specific conductivities of potassium hydroxide solutions for various concentrations and temperatures, *Int. J. Hydrogen Energy*, 2007, **32**, 359–364.

33 Electrical conductivity of aqueous solutions, in *CRC Handbook of Chemistry and Physics*, ed., J. R. Rumble, CRC Press/Taylor & Francis, Boca Raton, FL, 102nd edn, 2021, (Internet Version).

34 C. H. Pyun and S. M. Park, In situ spectroelectrochemical studies on anodic oxidation of copper in alkaline solution, *J. Electrochem. Soc.*, 1986, **133**, 2024–2030.

35 H. H. Strehblow and B. Titze, The investigation of the passive behaviour of copper in weakly acid and alkaline solutions and the examination of the passive film by esca and ISS, *Electrochim. Acta*, 1980, **25**, 839–850.

36 B. Miller, Split-ring disk study of the anodic processes at a copper electrode in alkaline solution, *J. Electrochem. Soc.*, 1969, **116**, 1675–1680.

37 M. Scherzer, F. Girgsdies, E. Stotz, M. G. Willinger, E. Frei, R. Schlögl, U. Pietsch and T. Lunkenbein, Electrochemical Surface Oxidation of Copper Studied by *in Situ* Grazing Incidence X-ray Diffraction, *J. Phys. Chem. C*, 2019, **123**, 13253–13262.

38 J. B. He, D. Y. Lu and G. P. Jin, Potential dependence of cuprous/cupric duplex film growth on copper electrode in alkaline media, *Appl. Surf. Sci.*, 2006, **253**, 689–697.

39 J. Ambrose, R. G. Barradas and D. W. Shoesmith, Investigations of copper in aqueous alkaline solutions by cyclic voltammetry, *J. Electroanal. Chem. Interfacial Electrochem.*, 1973, **47**, 47–64.

40 J. M. M. Droog, C. A. Alderliesten, P. T. Alderliesten and G. A. Bootsma, Initial stages of anodic oxidation of polycrystalline copper electrodes in alkaline solution, *J. Electroanal. Chem. Interfacial Electrochem.*, 1980, **111**, 61–70.

41 M. J. Dignam and D. B. Gibbs, Anodic oxidation of copper in alkaline solution, *Can. J. Chem.*, 1970, **48**, 1242–1250.

42 D. W. Shoesmith, S. Sunder, M. G. Bailey, G. J. Wallace and F. W. Stanchell, Anodic oxidation of copper in alkaline solutions: Part IV. Nature of the passivating film, *J. Electroanal. Chem. Interfacial Electrochem.*, 1983, **143**, 153–165.

43 S. Fletcher, R. G. Barradas and J. D. Porter, The anodic oxidation of copper amalgam and polycrystalline copper electrodes in LiOH solution, *J. Electrochem. Soc.*, 1978, **125**, 1960–1968.

44 S. Dong, Y. Xie and G. Cheng, Cyclic voltammetric and spectroelectrochemical studies of copper in alkaline solution, *Electrochim. Acta*, 1992, **37**, 17–22.

45 S. M. Abd el Haleem and B. G. Ateya, Cyclic voltammetry of copper in sodium hydroxide solutions, *J. Electroanal. Chem. Interfacial Electrochem.*, 1981, **117**, 309–319.

46 R. P. Vasquez, $CaCO_3$ by XPS, *Surf. Sci. Spectra*, 1998, **5**, 273.

47 I. Platzman, R. Brener, H. Haick and R. Tannenbaum, Oxidation of Policrystalline Copper Thin Films at Ambient Conditions, *J. Phys. Chem. C*, 2008, **112**, 1101–1108.

48 M. Biesinger, Advanced analysis of copper X-ray photoelectron spectra, *Surf. Interface Anal.*, 2017, **49**, 1325–1334.

49 X. Deng, A. Verdaguer, T. Herranz, Ch Weis, H. Bluhm and M. Salmeron, Surface Chemistry of Cu in the Presence of CO_2 and H_2O, *Langmuir*, 2008, **24**, 9474–9478.

50 M. Favaro, H. Xiao, T. Cheng, W. A. Goddard III, J. Yano and E. J. Crumlin, Subsurface oxide plays a critical role in CO2 activation by Cu(111) surfaces to form chemisorbed CO2, the first step in reduction of CO2, *Proc. Natl. Acad. Sci. U. S. A.*, 2017, **114**, 6706–6711.

51 M. Macías-Montero, C. López-Santos, A. N. Filippin, V. J. Rico, J. P. Espinós, J. Fraxedas, V. Pérez-Dieste, C. Escudero, A. R. González-Elipe and A. Borrás, In Situ Determination of the Water Condensation Mechanisms on Superhydrophobic and Superhydrophilic Titanium Dioxide Nanotubes, *Langmuir*, 2017, **33**, 6449–6456.

52 J. Fraxedas, M. Schütte, G. Sauthier, M. Tallarida, S. Ferrer, V. Carlino and E. Pellegrin, In situ XPS analysis of the electronic structure of silicon and titanium thin films exposed to low-pressure inductively-coupled RF plasma, *Appl. Surf. Sci.*, 2021, **542**, 148684.

53 S. Gates-Rector and T. Blanton, The Powder Diffraction File: a quality materials characterization database, *Powder Diffr.*, 2019, **34**, 352–360.

54 J. Wang, L. Zhu, L. Ji and Z. Chen, Preparation of nanostructured Cu(OH)2 and CuO electrocatalysts for water oxidation by electrophoresis deposition, *J. Mater. Res.*, 2018, **33**, 581–589.
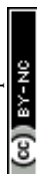
55 C. Li, H. Yamahara, Y. Lee, H. Tabata and J. J. Delaunay, CuO nanowire/microflower/nanowire modified Cu electrode with enhanced electrochemical performance for non-enzymatic glucose sensing, *Nanotechnology*, 2015, **26** 305503.

56 L. De Los Santos Valladares, D. Hurtado Salinas, A. Bustamante Dominguez, D. Acosta Najarro, S. I. Khondaker, T. Mitrelias, C. H. W. Barnes, J. Albino Aguiar and Y. Majima, Crystallization and electrical resistivity of Cu$_2$O and CuO obtained by thermal oxidation of Cu thin films on SiO$_2$/Si substrates, *Thin Solid Films*, 2012, **520**, 6368–6374.

57 A. A. Ogwu, T. H. Darma and E. Bouquerel, Electrical resistivity of copper oxide thin films prepared by reactive magnetron sputtering, *Mater. Manufac. Eng.*, 2007, **24**, 172–177.